

## Assessing Stretched-Vortex Subgrid-Scale Models in Finite Volume Methods for Unbounded Turbulent Flows

**Sean Walters (corresponding author) · Xinfeng Gao · Hans Johansen · Stephen Guzik**

Received: 20 April 2020 / Accepted: 9 August 2020

**Abstract** Simulations of complex, compressible, high-Reynolds-number flows require high-fidelity physics and turbulence models to be appropriately coupled with strong numerical regularization methods. Obtaining grid-independent and scheme-independent solutions of these flows when using both explicit turbulence models and additional numerical regularization is especially important for further testing and development of accurate physics models. To this end, the current study investigates the interaction between the stretched-vortex subgrid-scale model and both the fourth-order piecewise parabolic limiter and a fifth-order upwinding interpolation (or hyperviscosity). It is demonstrated that computing the subgrid-scale kinetic energy estimate for the stretched-vortex model at a coarser resolution than

---

This research was supported by Department of Defense United States Air Force (DOD-USAFAir Force) under the award number FA9550-18-1-0057. This material is partly based upon work at Lawrence Berkeley National Laboratory (LBNL) supported by the U.S. Department of Energy, Office of Science, Advanced Scientific Computing Research, under contract number DE-AC02-05CH11231. This research was supported by the National Science Foundation under the award number 1723191.

---

S. Walters (corresponding author)  
Computational Fluid Dynamics and Propulsion Laboratory, Colorado State University, Fort Collins, CO 80523, USA  
Tel.: 970-491-7545  
Fax: 970-491-3827  
E-mail: walters2@rams.colostate.edu

X. Gao  
Computational Fluid Dynamics and Propulsion Laboratory, Colorado State University, Fort Collins, CO 80523, USA

H. Johansen  
Applied Numerical Algorithms Group, Lawrence Berkeley National Laboratory, Berkeley, CA 94720, USA

S. Guzik  
Computational Fluid Dynamics and Propulsion Laboratory, Colorado State University, Fort Collins, CO 80523, USA

the base mesh provides results which are independent of the use of numerical regularization techniques. This is shown to be the case for a temporally-evolving shear-layer, the inviscid Taylor-Green vortex problem, and a decaying, homogeneous turbulent flow.

**Keywords** High-Order Finite-Volume Methods · Large-Eddy Simulation · Stretched-Vortex Turbulence Model · High-Reynolds-Number Flows

## 1 Introduction

Many flows of engineering interest are turbulent and inherently multiscale. Numerically resolving all scales in a high-Reynolds-number turbulent flow is challenging with today's computational capabilities. However, large-eddy simulation (LES) is a promising alternative to direct numerical simulations (DNS) in that it solves large scales while modeling small-scale effects to provide a solution acceptable for many engineering requirements. The approach is logical when rate-limiting processes happen at the larger resolved scales [1]. Even so, defining and modeling the small scales becomes one of the key issues in LES.

The typical LES definition of small scales begins by separating the original solution field,  $\phi$ , into representable scales,  $\bar{\phi}$ , and unrepresentable scales,  $\phi'$ , by means of a standard LES low-pass filter operator, the convolution operator,

$$G \star \phi = \bar{\phi}(\mathbf{x}, t) = \int_{-\infty}^{\infty} \int_{-\infty}^{\infty} \phi(\boldsymbol{\xi}, \tau) G(\mathbf{x} - \boldsymbol{\xi}, t - \tau) d\tau d\boldsymbol{\xi}, \quad (1)$$

where  $\mathbf{x}$  and  $\boldsymbol{\xi}$  are space,  $t$  and  $\tau$  are time, and  $G$  is the filter kernel. In general, LES simulations rarely define or use the filter kernel,  $G$ , explicitly. Rather, an implicit filter arises from the combined effects of the discretization, the numerical scheme, and any subgrid-scale (SGS) models used. This study assumes an implicitly defined Favre-averaged filter where Favre-filtered velocity,  $\tilde{\mathbf{u}}$ , is defined as mass-weighted momentum,  $\tilde{\mathbf{u}} = \bar{\rho}\bar{\mathbf{u}}/\bar{\rho}$ , with  $\rho$  being density. It is also assumed that the filter kernel size is equivalent to the cell size of the grid on which the SGS model is computed. As noted below, this does not necessarily correspond to the cell size of the grid on which the solution field is stored and updated.

As a result of the filtering process, all filtered nonlinear quantities must be modeled in terms of the individually filtered components. Explicitly modeled LES incorporates models developed for these filtered nonlinear terms, while implicit LES (ILES) relies on carefully designed characteristics of the numerical algorithm (e.g. numerical regularization or dissipation) to provide the necessary modeling [2–7]. The present study tests both ILES and explicitly modeled LES. The explicit LES model utilized is the stretched-vortex SGS model [8]. This structural model has provided results consistent with experimental data for very-high-Reynolds-number flows [9]. Numerical regularization in the form of either the piecewise parabolic method (PPM) limiter or hyperviscosity (introduced by fifth-order upwind face-value interpolation) provides the basis of ILES simulations performed within this study.

The goal of the present study is to combine numerical regularization and explicit LES models in a compatible manner and, if possible, achieve grid-independence and scheme-independence of large-scale solution data. Future studies of high-speed,

compressible, turbulent, reacting flows will require strong stabilization mechanisms independent of whether an explicit turbulence model is utilized. If the PPM limiter and hyperviscosity sufficiently simulate high-Reynolds-number turbulence, explicit turbulence models are unnecessary and would only increase computational cost. However, if an explicit model is required to achieve grid-independence of large-scale solution information, the turbulence model and the numerical regularization must interact in a compatible manner (i.e. each acts only where necessary). To achieve this, the current study computes the turbulence model terms on a coarsened solution field and then interpolates the model to the original solution field governed by the LES equations. This study uses a high-order finite-volume method (FVM) with adaptive mesh refinement (AMR) as a natural environment in which to test the coarsened SGS model computation.

Throughout this study, the Favre-filtered equations describing a compressible fluid flow, i.e. the conservation of mass ( $\rho$ ), momentum ( $\rho\mathbf{u}$ ), and energy ( $\rho e$ ), are considered. These equations are given as follows:

$$\frac{\partial \bar{\rho}}{\partial t} + \nabla \cdot (\bar{\rho}\tilde{\mathbf{u}}) = 0 , \quad (2)$$

$$\frac{\partial}{\partial t} (\bar{\rho}\tilde{\mathbf{u}}) + \nabla \cdot (\bar{\rho}\tilde{\mathbf{u}}\tilde{\mathbf{u}}^\top + \mathbf{I}\bar{p}) = \nabla \cdot (\tilde{\boldsymbol{\tau}} - \tilde{\boldsymbol{\tau}}_{sgs}) , \quad (3)$$

$$\frac{\partial}{\partial t} (\bar{\rho}\tilde{e}) + \nabla \cdot (\bar{\rho}\tilde{\mathbf{u}}\tilde{e} + \tilde{\mathbf{u}}\bar{p}) = \nabla \cdot (\tilde{\boldsymbol{\tau}} \cdot \tilde{\mathbf{u}} - \tilde{\mathbf{q}}) - \nabla \cdot (\tilde{\mathbf{E}}_{sgs_1} + \tilde{\mathbf{E}}_{sgs_2} - \tilde{\mathbf{E}}_{sgs_3}) , \quad (4)$$

$$\bar{p} = (\gamma - 1) \left( \bar{\rho}\tilde{e} - \frac{1}{2}\bar{\rho}\tilde{\mathbf{u}} \cdot \tilde{\mathbf{u}} - \tilde{\mathbf{E}}_{sgs_4} \right) , \quad (5)$$

$$\tilde{\boldsymbol{\tau}}_{sgs} = \bar{\rho} \left[ \widetilde{\mathbf{u}\mathbf{u}^\top} - \widetilde{\tilde{\mathbf{u}}\tilde{\mathbf{u}}^\top} \right] , \quad (6)$$

$$\tilde{\mathbf{E}}_{sgs_1} = \bar{\rho} [\widetilde{\mathbf{u}e} - \widetilde{\mathbf{u}\tilde{e}}] , \quad \tilde{\mathbf{E}}_{sgs_2} = \widetilde{\mathbf{u}p} - \widetilde{\mathbf{u}\bar{p}} , \quad \tilde{\mathbf{E}}_{sgs_3} = \widetilde{\boldsymbol{\tau} \cdot \mathbf{u}} - \widetilde{\boldsymbol{\tau} \cdot \tilde{\mathbf{u}}} , \quad (7)$$

$$\tilde{\mathbf{E}}_{sgs_4} = \frac{1}{2}\bar{\rho} [\widetilde{\mathbf{u} \cdot \mathbf{u}} - \widetilde{\mathbf{u} \cdot \tilde{\mathbf{u}}}] , \quad (8)$$

where  $\mathbf{I}$  is the identity matrix and  $\gamma$  is the specific-heat ratio of the fluid under consideration. The fluid is assumed to be a Newtonian, calorically perfect, ideal gas with heat flux,  $\tilde{\mathbf{q}}$ , approximated by Fourier's law

$$\tilde{\mathbf{q}} = -\kappa \nabla \widetilde{T} , \quad (9)$$

where  $\kappa$  is the thermal conductivity of the fluid, and  $\widetilde{T}$  is the Favre-averaged temperature. Additionally, the molecular stress,  $\tilde{\boldsymbol{\tau}}$ , is modeled by

$$\tilde{\boldsymbol{\tau}} = 2\mu \left( \tilde{\mathbf{S}} - \frac{1}{3}(\nabla \cdot \tilde{\mathbf{u}})\mathbf{I} \right) , \quad \tilde{\mathbf{S}} = \frac{1}{2} \left( \nabla \tilde{\mathbf{u}} + (\nabla \tilde{\mathbf{u}})^\top \right) , \quad (10)$$

where  $\mu$  is the molecular viscosity of the fluid. For the present study, it is assumed that  $\tilde{\mathbf{E}}_{sgs_3}$  is too small to necessitate modeling.

The rest of the paper is organized as follows. Section 2 details the stretched-vortex model as implemented in the current study. Section 3 describes the high-order FVM algorithm in which the stretched-vortex model is implemented and tested. The test cases and data processing details are presented in Section 4. The results and discussion of simulations performed in the current study are presented in Section 5. Finally, Section 6 wraps up the study with conclusions and recommendations for future research.

## 2 Stretched-Vortex Turbulence Model

The stretched-vortex (SV) SGS model, is a structural LES model and is based on the assumption that, at high Reynolds numbers and sufficiently small length scales, stretched vortex tubes dominate the flow physics [8, 10].

The model closes the filtered momentum equation, Eq. (3), using the SGS kinetic energy,  $K$ , and the SGS vortex orientation unit-vector,  $\mathbf{e}^v$ ,

$$\left( \widetilde{\mathbf{u}\mathbf{u}^\top} - \tilde{\mathbf{u}}\tilde{\mathbf{u}}^\top \right) = K \left( \mathbf{I} - \mathbf{e}^v (\mathbf{e}^v)^\top \right) . \quad (11)$$

Requiring  $K \geq 0$ ,  $\mathbf{e}^v$  alone determines whether the SV model is dissipative or anti-dissipative. The present study uses Misra and Pullin’s “model 1b” [8], which depends on the resolved vorticity vector,  $\mathbf{e}^\omega$ , and the eigenvector,  $\mathbf{e}^{\lambda_3}$ , associated with the largest positive eigenvalue,  $\lambda_3$ , of the strain-rate tensor,  $\tilde{\mathbf{S}}$ . A weighting factor,  $\sigma$ , controls the influence of each vector in the model,

$$\mathbf{e}^v (\mathbf{e}^v)^\top = \sigma \mathbf{e}^{\lambda_3} (\mathbf{e}^{\lambda_3})^\top + (1 - \sigma) \mathbf{e}^\omega (\mathbf{e}^\omega)^\top . \quad (12)$$

Using  $\sigma = 1$  guarantees a dissipative model [11–13], while incorporating  $\mathbf{e}^\omega$  decreases dissipation [14]. Throughout the present study, all simulations employing the SV model use  $\sigma = 1$ .

Among the proposed models for  $K$  [8, 15, 12, 16, 11], the model used by Chung and Pullin [11] is applied in this study. The model requires the evaluation of the incomplete gamma function,  $\Gamma[\cdot]$ , the grouped Kolmogorov constant,  $\mathcal{K}'_0$ , and a cutoff wavenumber,  $\kappa_c$ , and has the form

$$K = \frac{1}{2} \mathcal{K}'_0 \Gamma \left[ -\frac{1}{3}, \kappa_c^2 \right] . \quad (13)$$

The cutoff wavenumber,  $\kappa_c$ , is computed using

$$\kappa_c = \frac{\pi}{\Delta_c} \sqrt{\frac{2\nu}{3|\tilde{a}|}} , \quad \tilde{a} = (\mathbf{e}^{\lambda_3})^\top \tilde{\mathbf{S}} \mathbf{e}^{\lambda_3} , \quad \nu = \frac{\mu}{\bar{\rho}} , \quad \Delta_c = (\Delta x \Delta y \Delta z)^{1/3} . \quad (14)$$

The Kolmogorov constant,  $\mathcal{K}'_0$  is given by

$$\mathcal{K}'_0 = \frac{\{F_2\}}{\{Q(\kappa_c, d)\}} . \quad (15)$$

In Eq. (15),  $\{\cdot\}$  is an ensemble average of the variables over a spatial domain,  $\Omega$ , encompassing  $N$  points,  $\mathbf{x}_i$ , neighboring  $\mathbf{x}_0$

$$\{\phi\} = \frac{1}{N} \sum_{\mathbf{x}_i \in \Omega ; \mathbf{x}_i \neq \mathbf{x}_0} \phi(\mathbf{x}_0, \mathbf{x}_i) , \quad (16)$$

where, in this study,  $N = 26$ .  $F_2$  is the second-order structure function

$$F_2 = (\tilde{\mathbf{u}}(\mathbf{x}_0) - \tilde{\mathbf{u}}(\mathbf{x}_i)) \cdot (\tilde{\mathbf{u}}(\mathbf{x}_0) - \tilde{\mathbf{u}}(\mathbf{x}_i)) . \quad (17)$$

Additionally,  $Q$  is a weighting evaluated over all wavenumbers,  $k$ , given by

$$Q(\kappa_c, d) = 4 \int_0^{\kappa_c} k^{-5/3} \exp(-k^2) \left( 1 - J_0 \left( \frac{k}{\kappa_c} \pi d \right) \right) dk , \quad (18)$$

where  $J_0$  is the zeroth-order Bessel function of the first kind, and  $d$  is the planar distance from the cell center to the SGS vortex axis

$$d = \frac{r}{\Delta_c} \quad , \quad r^2 = [(\mathbf{x}_0 - \mathbf{x}_i) \cdot (\mathbf{x}_0 - \mathbf{x}_i)] - [(\mathbf{x}_0 - \mathbf{x}_i) \cdot \mathbf{e}^{\lambda_3}]^2 . \quad (19)$$

Efficient means of computing  $\mathcal{K}'_0$ ,  $\Gamma[\cdot]$ , and the eigenvalues/eigenvectors are presented by Voelkl and others [15–17].

In addition to closing the filtered momentum equation, Eq. (3), the current study models  $\tilde{\mathbf{E}}_{sgs_1}$  and  $\tilde{\mathbf{E}}_{sgs_2}$  in the filtered energy equation, Eq. (4), following the methodology presented by Kosovic, et al. [18] and Hill, et al. [19]. The results presented throughout this study do not use the model of Kosovic, et al. [18] and Hill, et al. [19] for the SGS stress correction,  $\tilde{\mathbf{E}}_{sgs_4}$ , in the pressure computation of Eq. (5). Comparisons of decaying turbulence simulations with and without the pressure correction showed no observable difference between the two in globally summed quantities and in energy spectra. For these low Mach number flows, this observation is expected.

### 3 Numerical Framework

#### 3.1 FVM Algorithm: Chord

All results presented in this study are obtained using the FVM algorithm, Chord [20–24], built upon the highly parallelizable (scaling to at least  $1 \times 10^5$  cores) AMR framework Chombo [25]. Chord solves the governing equations for transient, compressible, turbulent, reacting and non-reacting fluid flows with complex geometry. It has been designed to achieve high levels of accuracy and performance for turbulence and combustion simulations on modern high-performance computing architecture. For smooth flows, Chord is fourth-order accurate in space and time (using the standard four-stage Runge Kutta time-marching method) [20–24]. For flows with strong discontinuities (e.g. shocks or detonation waves), the PPM limiter [26, 27] is used for stability. Chord is capable of additional stabilization by hyperviscosity through fifth-order face-value interpolations. Chord's turbulence modeling capabilities include unsteady Reynolds-averaged Navier-Stokes (URANS), LES, and DNS. Additionally, Chord utilizes AMR in space and subcycling in time and accommodates complex geometry while preserving free-stream conditions using generalized coordinate transformations.

In the present study, all spatially discrete operators are fourth-order accurate by default. However, numerical stabilization in the form of either the PPM limiter or hyperviscosity is tested in conjunction with the SV LES model.

#### 3.2 Fifth-order interpolation/hyperviscosity

In FVMs, flux evaluations at the faces of a computational cell are essential and require knowledge of face values. Reconstructing solution variables at cell faces is one of the fundamental operations in the algorithm and is a major difficulty in terms of stability. Low-dissipation, high-order, centered interpolations can create

spurious, high-frequency solution content and allow it to grow, especially near unresolved solution gradients. Adding a high-order viscosity term to the interpolation through a spatially-biased interpolant can help alleviate spurious high-frequency content [28].

Interpolating the face-averaged primitive state,  $\langle \mathbf{W} \rangle_{i+\frac{1}{2}\mathbf{e}^d}$ , from the cell-averaged primitive state,  $\langle \mathbf{W} \rangle_i$ , follows the process described in previous literature [20, 21]. A cell index is denoted by  $i$  on an integer lattice and  $\mathbf{e}^d$  is a unit-vector in direction  $d$ . A cell face is reached by a shift of  $1/2$ . A four-cell, fourth-order, centered approximation to  $\langle \mathbf{W} \rangle_{i+\frac{1}{2}\mathbf{e}^d}$  is given by

$$\langle \mathbf{W} \rangle_{i+\frac{1}{2}\mathbf{e}^d}^{(4)} = \frac{7}{12} (\langle \mathbf{W} \rangle_i + \langle \mathbf{W} \rangle_{i+\mathbf{e}^d}) - \frac{1}{12} (\langle \mathbf{W} \rangle_{i-\mathbf{e}^d} + \langle \mathbf{W} \rangle_{i+2\mathbf{e}^d}), \quad (20)$$

while the right-biased, five-cell, fifth-order approximation is provided by

$$\begin{aligned} \langle \mathbf{W} \rangle_{i+\frac{1}{2}\mathbf{e}^d,R}^{(5)} &= \frac{1}{60} (-3\langle \mathbf{W} \rangle_{i-\mathbf{e}^d} + 27\langle \mathbf{W} \rangle_i + 47\langle \mathbf{W} \rangle_{i+\mathbf{e}^d} - 13\langle \mathbf{W} \rangle_{i+2\mathbf{e}^d}) \\ &\quad + \frac{1}{60} (2\langle \mathbf{W} \rangle_{i+3\mathbf{e}^d}) . \end{aligned} \quad (21)$$

A reflection of Eq. (21) about the face provides a left-biased interpolation. Using both the left and right-biased values, the final face value is the solution of a Riemann problem.

Examining the difference between the two interpolations reveals the high-order, cell-centered numerical dissipation term present in the fifth-order interpolant

$$\begin{aligned} \langle \mathbf{W} \rangle_{i+\frac{1}{2}\mathbf{e}^d,R}^{(5)} - \langle \mathbf{W} \rangle_{i+\frac{1}{2}\mathbf{e}^d}^{(4)} &= \\ \frac{1}{30} (\langle \mathbf{W} \rangle_{i-\mathbf{e}^d} - 4\langle \mathbf{W} \rangle_i + 6\langle \mathbf{W} \rangle_{i+\mathbf{e}^d} - 4\langle \mathbf{W} \rangle_{i+2\mathbf{e}^d} + \langle \mathbf{W} \rangle_{i+3\mathbf{e}^d}) &\quad (22) \\ \approx \frac{\Delta x^4}{30} \frac{\partial^4}{\partial x^4} (\langle \mathbf{W} \rangle_{i+\mathbf{e}^d}) . \end{aligned}$$

It is through the high-order numerical dissipation term that the highest frequency content is detected and controlled.

### 3.3 Piecewise Parabolic Method

The high-order piecewise parabolic method (PPM) is an extension of Godunov's method [29, 26, 27]. Essentially, the PPM consists of two main steps. First, face values are interpolated using high-order finite-difference approximations based on the cell-averaged values. If necessary, the interpolants are limited to ensure monotonicity. Second, a parabolic profile is constructed in each cell and constrained to keep it monotone. If the local extremum is smooth, as determined by checking adjacent second derivatives, the limiter is not applied. A third-derivative condition is also checked to avoid limiting perturbations of a cubic in multidimensional problems [27]. The PPM scheme delivers a more accurate representation of spatial gradients of smooth flows and a steeper representation of discontinuities. Additional techniques such as artificial dissipation and slope flattening are applied at shocks to suppress unwanted numerical oscillations. In the limit of a complete flattening, the scheme recovers the first-order Godunov method locally near the discontinuities. In the present study, the PPM scheme is implemented closely following the work by McCorquodale and Colella [27].

### 3.4 Numerical Implementation of the SV SGS Model

When applying the SV SGS model at a coarser length scale,  $\Delta_f$ , than the grid filter,  $\Delta x$ , existing AMR infrastructure is used within Chord. As shown in Fig. 1, the cell-averaged primitive state on the original fine mesh at cell-index  $i$ ,  $\langle \mathbf{W} \rangle_i^f$ , is averaged to a coarser mesh,  $\langle \mathbf{W} \rangle_i^c$ . The fine mesh has cell spacing  $\Delta x$ . Following the

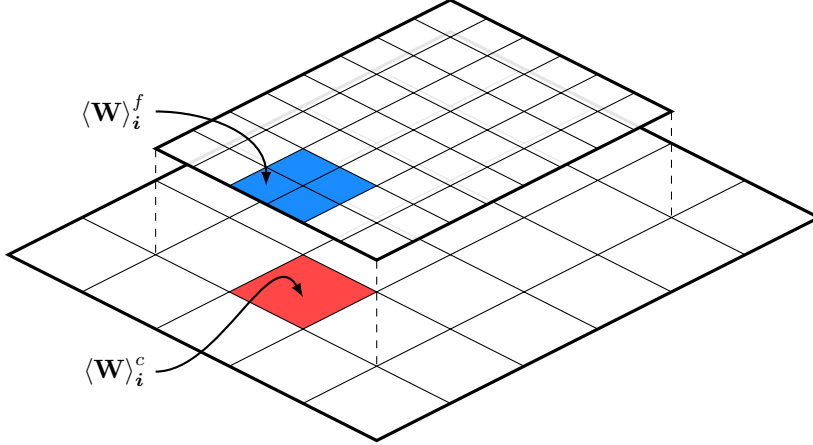


**Fig. 1** Coarsened SGS kinetic energy estimate (example demonstrates  $\Delta_f = 2\Delta x$ )

averaging procedure, the coarse cell-averaged value,  $\langle \mathbf{W} \rangle_i^c$ , is deconvolved to obtain the cell-centered value,  $\mathbf{W}_i^c$ , to fourth-order accuracy using the deconvolution [27]

$$\mathbf{W}_i^c = \langle \mathbf{W} \rangle_i^c - \sum_d \frac{h_d^2}{24} \frac{\partial^2 \langle \mathbf{W} \rangle_i^c}{\partial x_d^2}, \quad (23)$$

where  $h$  is the cell spacing of the grid level. Working with the cell-centered state as opposed to the cell-averaged state preserves the order-of-accuracy of the numerical scheme and the SGS energy estimate in smoothly varying solution fields even when computing nonlinear terms. To use the cell-averaged quantities during the computation of nonlinear terms would not preserve the scheme's order-of-accuracy in nonlinearly-evolving smooth regions of the flow unless rather complicated product-rules of averages were utilized. On the coarser mesh, with cell spacing  $\Delta_f$ , the SGS kinetic energy estimate is computed using  $\mathbf{W}_i^c$  and then interpolated to the original mesh. From here,  $\langle K_{SGS} \rangle^f$  is interpolated to the cell faces. On the cell faces, the orientation model is computed using  $\mathbf{W}_i^f$  and combined with  $K_{SGS}^f$  to obtain a conservative SGS momentum flux. The detailed steps as presented in an algorithm format are as follows:

1. Average the fine cell-averaged primitive state to a coarser mesh and deconvolve it to obtain the coarse cell-centered primitive state:

$$\langle \mathbf{W} \rangle_i^f \rightarrow \langle \mathbf{W} \rangle_i^c \rightarrow \mathbf{W}_i^c$$

2. Compute the coarsened cell-centered SGS kinetic energy estimate from the cell-centered primitive state and average it over a coarse cell:

$$\mathbf{W}_i^c \rightarrow (K_{SGS})_i^c \rightarrow \langle K_{SGS} \rangle_i^c$$

3. Interpolate the cell-averaged SGS kinetic energy estimate to the fine mesh:

$$\langle K_{SGS} \rangle_i^c \rightarrow \langle K_{SGS} \rangle_i^f$$

4. Interpolate the fine cell-averaged SGS kinetic energy estimate to the cell faces and deconvolve it to obtain the fine face-centered SGS kinetic energy estimate:

$$\langle K_{SGS} \rangle_i^f \rightarrow \langle K_{SGS} \rangle_{i+\frac{1}{2}\epsilon^d}^f \rightarrow (K_{SGS})_{i+\frac{1}{2}\epsilon^d}^f$$

5. Compute the fine face-centered turbulent flux using the interpolated SGS kinetic energy estimate and the orientation model computed on the fine mesh with fine mesh data.

As complex as this appears, even without optimizing the computational implementation, the SGS model costs less than 10% of the computation time when the coarsening ratio is 4 ( $\Delta_f = 4\Delta_x$ ), and approximately 35% of the computation time when  $\Delta_f = \Delta_x$  for a three-dimensional simulation. In other words, applying the model at a coarser scale reduces the expense of computing the nonlinear filtered terms.

Using  $\Delta_f > \Delta_x$  for the SV model has previously been tested, as in the study of Chung and Matheou [30]. Furthermore, it was conclusively demonstrated that grid-converged LES results are obtainable for high Reynolds number, practical flow simulations. The current study departs from the implementation methodology of Chung and Matheou in that the current study explicitly uses a coarser mesh when computing the SV model SGS kinetic energy estimate rather than implicitly incorporating the larger filter width through the  $\kappa_c$  parameter in Eqs. (13–15). This difference is utilized in order to enable the coupling of the SV model with numerical regularization. Without computing the SGS kinetic energy estimate on a coarser mesh, the smallest represented information necessary for the the SV model SGS kinetic energy calculation would still largely be affected by the numerical regularization. As a result, the model would still register too low of an SGS kinetic energy estimate, even with the increased filter-width size being incorporated into the computations through  $\kappa_c$ . The SV model was originally designed to match an explicitly defined SGS kinetic energy spectra to the smallest representable-scale kinetic energy. Using numerical regularization, it is expected that the scales used to match the SGS kinetic energy spectra should no longer reside near the grid-cutoff, but rather at the scales associated with the equivalent filter size of the LES system.

#### 4 Test Cases

Throughout this study, three cases test the concepts and algorithms. The first is a temporally-evolving mixing-layer [31,32,13], while the second case is the decaying, inviscid Taylor-Green vortex where the Reynolds number is infinity [33]. The last case is a decaying, homogeneous turbulence case based on the widely used Comte-Bellot and Corrsin experimental dataset of decaying, grid-generated turbulence [34].

#### 4.1 Time-Evolving Mixing-Layer

The time-evolving mixing-layer considered in the present study is configured as fully-periodic double-shear as shown in Fig. 2. The freestream velocities of streams

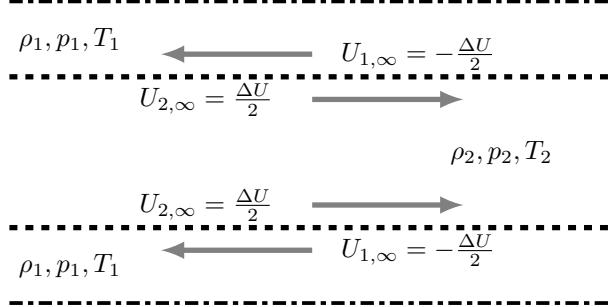


**Fig. 2** Configuration of the time-evolving double mixing-layer

1 and 2 are  $U_{1,\infty} = 34.03$  m/s and  $U_{2,\infty} = -U_{1,\infty}$ , respectively, and the freestream pressures and densities of both streams are identical. The flow has a Mach number,  $M$ , of 0.1 based on the arithmetic mean of  $|U_{1,\infty}|$  and  $|U_{2,\infty}|$ , a Prandtl number,  $\text{Pr} = 0.71$ , a specific heat ratio,  $\gamma = 1.4$ , and a Reynolds number of 11650, based on

$$Re_{\delta_\omega,0} = \frac{\rho|U_\infty|\delta_\omega}{\mu}, \quad (24)$$

where  $\delta_\omega$  is the initial vorticity thickness

$$\delta_\omega = \frac{1}{\rho_0} \int_{-L_y/2}^{L_y/2} \bar{\rho} \left( 1 - \frac{\tilde{u}^2}{(\Delta u/2)^2} \right) dy, \quad (25)$$

with  $L_y$  being the domain length in the shear-layer normal direction, and  $\Delta u$  being the magnitude of the difference between the two freestream velocities,  $\Delta u = |U_{2,\infty} - U_{1,\infty}|$ . The momentum thickness,  $\delta_\theta$ , is  $\delta_\omega/4$ . The computational domain size is,  $L_x \times L_y \times L_z = 137\delta_\theta \times 137\delta_\theta \times 68\delta_\theta$ . The meshes consist of coarse resolutions with  $64 \times 64 \times 32$  cells in the streamwise, shear-layer normal, and spanwise directions respectively, medium resolutions with  $128 \times 128 \times 64$  cells, and fine resolutions with  $256 \times 256 \times 128$  cells.

The velocities in each stream were sinusoidally perturbed and computed from a stream function in order to achieve an analytically divergence-free initial velocity field. This stream function is defined as

$$\Psi = \xi U_{1,\infty} \tanh \left( \frac{\xi}{2\delta_\theta} \right), \quad (26)$$

where the factor  $\xi$  is defined as

$$\xi = y + \exp(-\eta|y|) \left( \sum_i b_i \sin \left( \frac{2\pi\omega_i x}{L} + \phi_i \right) \right), \quad (27)$$

and the velocities are computed analytically as

$$u = \frac{\partial \Psi}{\partial y} , \quad v = -\frac{\partial \Psi}{\partial x} . \quad (28)$$

The  $i$ -th perturbation mode has phase shift  $\phi_i$ , wavenumber  $\omega_i$ , and magnitude  $b_i$ . The parameter  $\eta$  controls the decay rate of the perturbations in the shear-layer normal direction. For this study,  $\eta = 8\pi/L_y$ . Perturbation modes with  $\omega = 8, 4, 2$ , and  $1$  were chosen for the streamwise and spanwise directions. The dominant mode with  $\omega = 8$  was given  $b = 0.1(L_y/2)$  for the streamwise direction and  $b = 0.05(L_y/2)$  for the spanwise direction. All other perturbations were randomly provided magnitudes of either three percent or one percent of the half-domain height. Streamwise and spanwise phase shifts were randomly chosen. Density was initialized from the ideal gas law assuming constant pressure, identical freestream density values for both shear-layer streams, and using the Crocco-Busemann relation for temperature

$$\rho = \rho_0 \left[ 1 + \frac{1}{2} (\gamma - 1) M^2 \left( 1 - \tanh \left( \frac{\xi}{2\delta_\theta} \right) \right) \left( 1 + \tanh \left( \frac{\xi}{2\delta_\theta} \right) \right) \right] . \quad (29)$$

Pressure was initialized assuming a constant pressure profile with correction for the velocity perturbations

$$p = p_0 - \frac{1}{2} \rho_0 \left( \hat{u}^2 + 2\hat{u}U_0 \tanh \left( \frac{\xi}{2\delta_\theta} \right) + v^2 \right) (\gamma - 1) , \quad (30)$$

where  $\hat{u}$  is given by

$$\hat{u} = u - U_0 \tanh \left( \frac{\xi}{2\delta_\theta} \right) . \quad (31)$$

The double-shear problem provides an anisotropic-turbulence test case in which the turbulence is fed by a freestream, large-scale energy reservoir. This energy reservoir continually generates turbulence until the turbulence reaches the periodic boundaries, essentially mimicking a forced turbulence problem. At this point, the energy decays away. Although a relatively simple configuration, the double-shear case provides a test with flow features commonly encountered in real-world engineering problems. The large-scale anisotropy is common in almost any wall-bounded or jet-type flow as is the continual production of turbulent energy from large-scale flow features that persist for long time-periods. For these reasons, the time-evolving shear-layer has been a favorite for testing LES models and algorithms. The SV model has previously been tested with the time-evolving shear-layer by Mattner [13]. While Mattner used a Fourier spectral collocation scheme in the periodic streamwise and spanwise directions and an eighth-order finite-difference scheme in the slip-wall-bounded shear-layer normal direction, every coordinate direction in the present study uses the finite-volume discretization described in Section 3. Additionally, Mattner presented one-dimensional energy spectra while the current study presents three-dimensional energy spectra.

#### 4.2 Inviscid Taylor-Green Vortex

The Taylor-Green vortex flow is initialized in a fully-periodic cube of side-length  $D$  with a sinusoidal initial condition given by

$$u = -U_0 \sin\left(\frac{n\pi x}{D}\right) \cos\left(\frac{n\pi y}{D}\right) \sin\left(\frac{n\pi z}{D}\right) \quad (32)$$

$$v = U_0 \cos\left(\frac{n\pi x}{D}\right) \sin\left(\frac{n\pi y}{D}\right) \sin\left(\frac{n\pi z}{D}\right) \quad (33)$$

$$w = 0 \quad (34)$$

$$p = p_0 + \frac{\rho_0 U_0^2}{16} \left( \cos\left(\frac{2n\pi x}{D}\right) + \cos\left(\frac{2n\pi y}{D}\right) \right) \left( \cos\left(\frac{2n\pi z}{D}\right) + 2 \right) \quad (35)$$

$$\rho = \frac{p}{RT_0} = \frac{p\rho_0}{p_0} \quad (36)$$

where  $U_0$  is the velocity fluctuation magnitude and  $n$  is the number of vortices contained in the domain in each coordinate direction. The flow has a Mach number based on  $U_0$  of 0.1, a Prandtl number of 0.71, and a specific heat ratio  $\gamma = 1.4$ . Cell counts of  $64^3$ ,  $128^3$ , and  $256^3$  were used for all of the Taylor-Green vortex cases.

In the limit of infinite Reynolds number, the Taylor-Green vortex provides an ideal test of algorithmic components examined in this study. The vortex evolution begins with “vortex wrap-up”, eventually transitioning to a turbulent energy cascade process. It is apparent that all initial kinetic energy eventually resides at the subgrid-scale even though it is never dissipated in this inviscid problem. Once the kinetic energy resides at the subgrid-scale, it is indistinguishable from internal energy except through a model. As a result, the numerical algorithm must sufficiently dissipate represented-scale kinetic energy while correctly capturing the energy cascade process. This test case will demonstrate the dissipative characteristics of the algorithms when physical viscosity is absent.

#### 4.3 Decaying Homogeneous Turbulence

Decaying, grid-generated turbulence is a classic test of the capabilities of LES models and multiple experimental datasets are readily available for this case [35, 34, 36]. This particular study simulates the Comte-Bellot and Corrsin experiment [34] following the numerical procedure outlined by Rozema, et al. [37] and partially developed by Kang et al. [38].

The experimental case consists of a bulk flow,  $U_{\text{ref}}$ , of 10 m/s through a mesh with a spacing between wires,  $L_{\text{ref}}$ , of 0.0508 m. A characteristic time,  $\tau$ , is defined as

$$\tau = t \frac{U_{\text{ref}}}{L_{\text{ref}}} , \quad (37)$$

where  $t$  is the true physical time. If a reference-frame is chosen to convect with the flow, a change in spatial location can be correlated with a change in time in the convecting reference frame. Measurements of the one-dimensional energy spectra were performed at spatial locations corresponding with characteristic convecting reference frame times of  $\tau = 42, 98$ , and 171 after the generation of the turbulence

by the mesh. At the first measurement station,  $\sqrt{u_1^2}$  was measured to be 0.222 m/s and the Kolmogorov scale was determined to be  $2.94 \times 10^{-4}$  m.

To numerically simulate this case, a domain reference length,  $D_{\text{ref}}$ , was chosen as  $11L_{\text{ref}}$  and a local turbulent velocity reference value of  $u_{\text{ref}}$  was chosen as  $0.222\sqrt{3/2}$  m/s in order to match the experimental value of  $\sqrt{u_1^2}$ . All computational parameters were nondimensionalized by  $D_{\text{ref}}$  and  $u_{\text{ref}}$  as necessary. An algorithm-dependent, divergence-free initial condition with random phase shifts was fit to the energy spectrum measured at the first station ( $\tau = 42$ ). Each case was run with the algorithm specific initial condition from  $\tau = 0$  to  $\tau = 42$ . The resulting flow fields were each rescaled following the method proposed by Kang et al. [38] in order to act as the initial condition for the simulations in this particular study. In the present study, the cell-averaged field at  $\tau = 42$  was deconvolved using the same method as presented in McCorquodale and Colella [27] to obtain the point-value field that could be rescaled. Following the rescaling of the point values, the rescaled cell-averaged field was computed using a box-filter convolution operator. The rescaled fields were then used as initial conditions to run from  $\tau = 42$  to  $\tau = 171$ . The Reynolds number based on  $u_{\text{ref}}$  and the domain size was 10400. Meshes of size  $64^3$ ,  $128^3$ , and  $256^3$  are used for all decaying homogeneous turbulence simulations in the present study.

#### 4.4 Simulations and Data Analysis

A non-dimensional, characteristic time,  $\tau$ , is utilized for all the results presented. This “eddy turn-over” time is defined as

$$\tau = t \frac{U}{L} , \quad (38)$$

where  $U$  is a characteristic velocity and  $L$  is a characteristic length scale. For the shear-layer case, the characteristic time scale is computed from the arithmetic mean of the absolute values of the two stream velocities and the initial momentum thickness. For the inviscid Taylor-Green vortex the characteristic scales are chosen to be the turbulent velocity and the integral length scale, while for the decaying homogeneous turbulence case, these are the convective velocity and the mesh spacing. The shear-layer spectrum transitions to fully developed turbulence by  $\tau \approx 20$ . The decaying Taylor-Green cases transition to fully developed turbulence by  $\tau \approx 10$ . After this point, the kinetic energy decays away due to the energy cascade process.

The results of interest in this study are presented using the three-dimensional kinetic energy spectra from each case. All spectral data is computed from instantaneous flow data using the software package FFTW. To compute the three-dimensional energy spectra, the square of the Fourier-transformed velocity vector is shell-summed. The resulting kinetic energy is then normalized using the simulation domain volume and the initial sum of kinetic energy such that the sum of the kinetic energy presented in the spectrum plots is equal to unity at the start of the simulation. The wavenumber,  $k$ , is given with respect to the simulation domain such that  $k = 1$  is the largest wave mode fully contained in the periodic simulation domain.

For each of the test cases presented, the kinetic energy spectrum results are broken into five distinct parts gathered into two separate figures. The first column of the first figure for each test case compares the use of three different numerically regularized algorithms: the fourth-order centered discretization with the SV model (explicit LES), the fourth-order PPM algorithm (implicit LES), and the fifth-order algorithm (implicit LES). The second column of the first figure presents the coupling between the SV model and the last two numerical regularization techniques presented in the first column. This particular set demonstrates issues that arise from naive couplings of the LES SGS model with numerical regularization techniques (when  $\Delta_f = \Delta x$ ). For the third column, the SV model is used with and without numerical regularization and specifically utilizes the coarsening method proposed in this study ( $\Delta_f \neq \Delta x$ ). The second figure of kinetic energy spectrum for each simulation displays the comparison between the various schemes using the coarsened SV model at single mesh resolutions. The first row shows the kinetic energy spectra as previously described, while the second row displays the kinetic energy premultiplied by the wavenumber,  $k$ , and placed in a log-linear plot. This last presentation of the results is intended to specifically highlight the largest wave modes and demonstrate whether or not the simulation results are grid-converged. The first two columns of spectra in the first figure are intended to show the baseline performance of the algorithms presented. The last column of the first figure highlights grid-independence achieved by the coarsened SV model computation. The second figure highlights scheme-independence achieved by the coarsened SV model computation, in that all numerical regularization approaches converge to the same result.

## 5 Results and Discussion

### 5.1 Time-Evolving Mixing-Layer

The double-shear-layer results presented in this section consist of a three-dimensional kinetic energy spectra plot demonstrating the kinetic energy evolution in Fig. 3, vorticity contours demonstrating the flow evolution in Fig. 4, and three-dimensional kinetic energy spectra in Fig. 5–6.

As shown in Fig. 4, the double-shear-layer problem begins with the development of coherent vortices. These vortices rapidly break down and lead to full development of the kinetic energy spectrum by  $\tau \approx 20$  as seen with the use of the fourth-order centered discretization with the SV model and no numerical regularization in Fig. 3. The two layers continue to evolve in a turbulent manner and grow in the shear-layer normal direction until they begin interacting with one another at  $\tau \approx 35$ . Between  $\tau \approx 20$  and at least  $\tau \approx 80$ , the kinetic energy spectrum is in a quasi-steady state, mimicking artificially forced turbulence quite well. This quasi-steady state turbulence allows for the study of the various algorithms over long periods of time at moderate Reynolds numbers.

Examining Fig. 4 provides a means of visualizing the differences between using numerical regularization without the SV model and using the SV model with no additional numerical regularization. The first column presents the results from using the fourth-order PPM scheme with no turbulence model, while the second, third, and fourth columns present the results from using the SV model with  $\Delta_f =$

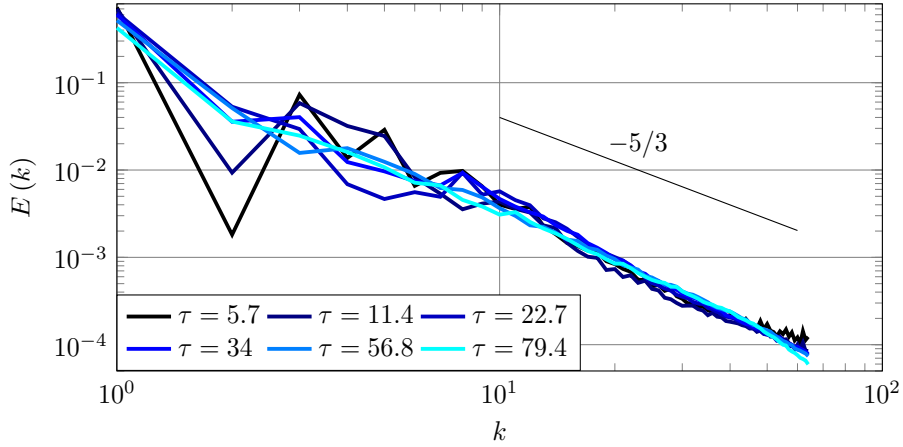
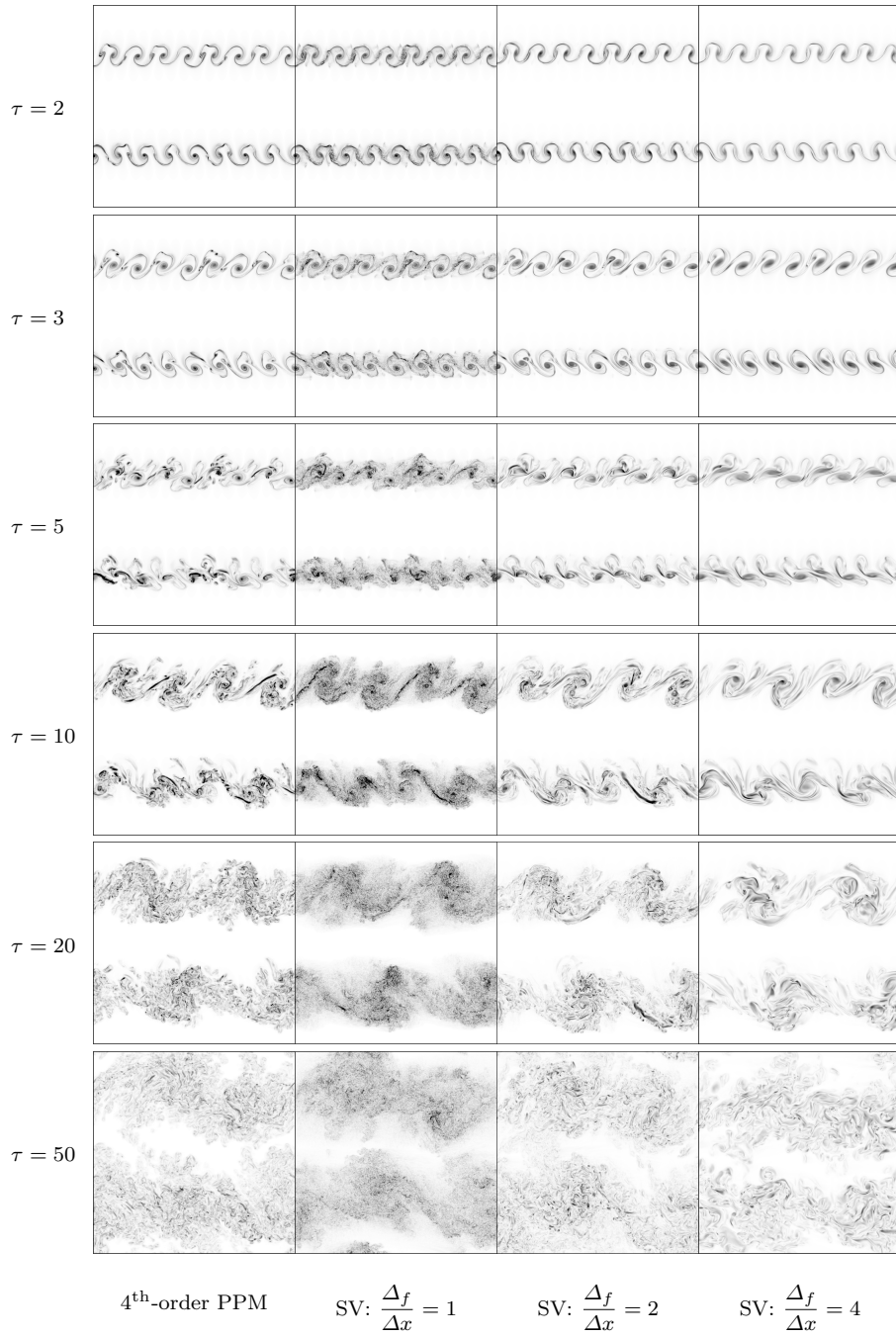


**Fig. 3** Double-shear-layer time evolution of kinetic energy spectrum using the fourth-order SV model and no numerical regularization on a  $128 \times 128 \times 64$  mesh with  $\Delta_f = \Delta x$

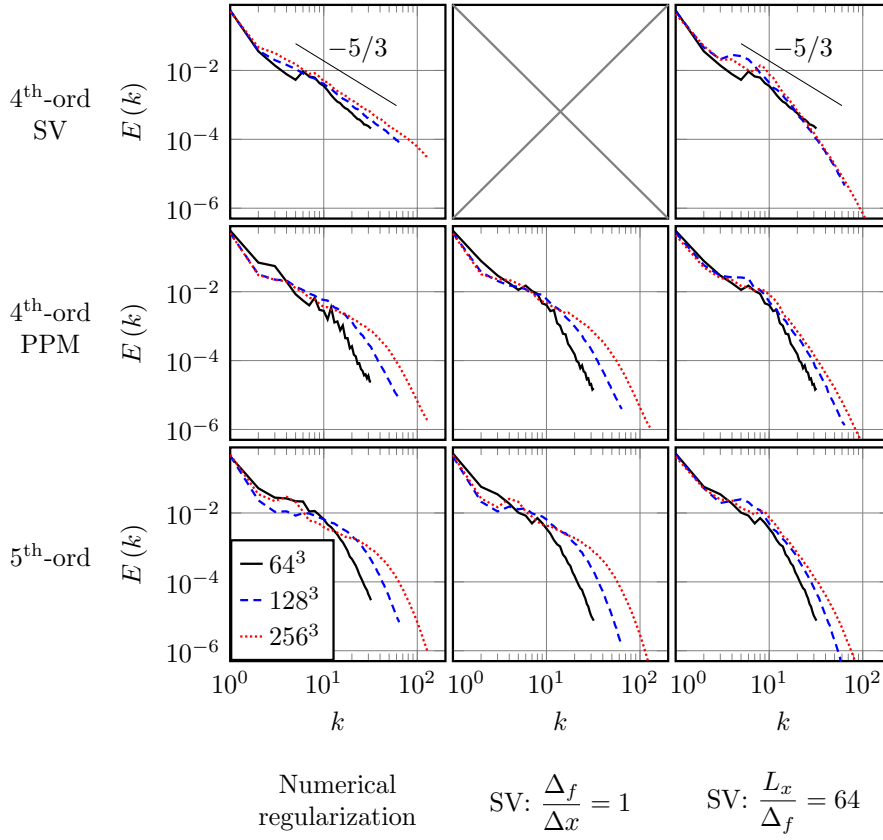
$\Delta x$ ,  $\Delta_f = 2\Delta x$ , and  $\Delta_f = 4\Delta x$  respectively. From the results of the first column, it is observed that the PPM method dampens most high-frequency solution content (as compared with the SV model results in the second column) while still allowing some small-scale flow features to develop. Examining column two of Fig. 4, it is readily apparent that the SV model with  $\Delta_f = \Delta x$  allows more high-frequency data to remain than the PPM method. However, as the coarsening factor of the SV model is increased beyond unity ( $\Delta_f > \Delta x$ ), the solution field retains less high-frequency content as displayed in columns three and four of Fig. 4. Instead, only the larger-scale vortices remain and the resolvability of the flow field increases. This increase in resolvability decreases the likelihood that poorly resolved fluctuations will contaminate the well-resolved large-scale information. It is also important to note that the overall structure of the largest-scale vortices remains relatively unchanged as the  $\Delta_f/\Delta x$  ratio is increased for the SV model. The SV model only removes more of the small scales as the  $\Delta_f/\Delta x$  ratio increases, allowing for the potential of grid-independent solutions.

Figure 5 presents a comparison of several schemes used to simulate the double-shear case. The first column is a comparison of three methods of numerical regularization: the fourth-order SV algorithm (first row), the PPM method (second row), and fifth-order interpolation/hyperviscosity (third row). The second column adds the SV model to the PPM method (row 2), and the biased interpolation (row 3). In the third column, the SV model is applied at different ratios of  $\Delta_f/\Delta x$  with constant  $\Delta_f$ .

The fourth-order centered discretization with the SV model, presented in the first column of row one of Fig. 5, shows more consistency in the largest scales with decreasing  $\Delta x$  than either of the other two numerically regularized schemes presented in the first column. It is evident that the fifth-order interpolation performs worse than the fourth-order PPM scheme when considering the largest scales. From these results, it would be natural to conclude that the fourth-order SV algorithm



**Fig. 4** Evolution of double-shear-layer vorticity magnitude from  $\tau = 2$  to  $\tau = 50$ , mesh size  $512 \times 512 \times 256$ . Rows from top to bottom display increasing simulation time while each column presents a different numerical scheme. The vorticity magnitude presented here is in grayscale contours ranging from white = 0 [ $\text{s}^{-1}$ ] to black = 75,000 [ $\text{s}^{-1}$ ]



**Fig. 5** Kinetic energy spectra of double-shear-layer case at  $\tau = 50$ . The first column presents three methods of numerical regularization: the SV model (row 1), the PPM method (row 2), and biased interpolation (row 3). The second column adds the SV model to the PPM method (row 2), and the biased interpolation (row 3). The final column presents the same schemes except with a fixed  $\Delta_f$  equivalent to  $1/64^{\text{th}}$  the streamwise length of the domain

should be used in this simulation, especially when strong numerical regularization techniques are unnecessary for a low Mach number flow such as this case. However, as this study provides one piece of a foundation for future simulations of high-speed, compressible, reacting turbulent flows, numerical regularization must be tested and compared with the fourth-order SV results. Additionally, it is apparent that none of these methods provides the grid-independent or scheme-independent solutions which are sought within this study.

As previously noted, column two of Fig. 5 displays the results of naively coupling the SV model with the last two numerically regularized schemes of the first column. If the SV model with no additional numerical regularization performs somewhat well, it may be anticipated that adding the SV model to the fourth-order PPM method or the fifth-order interpolation would improve these results.

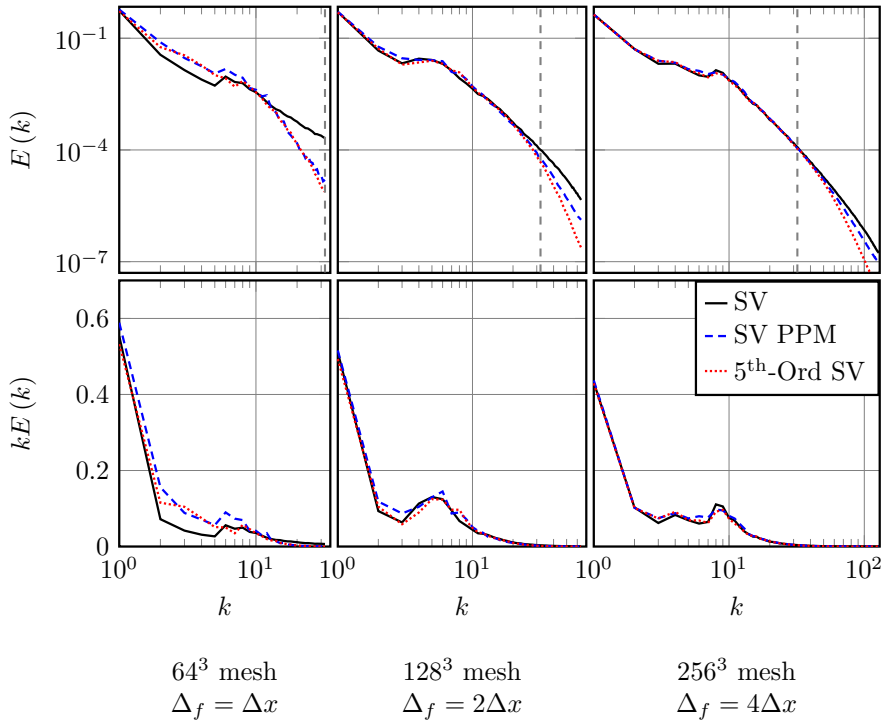


**Fig. 6** Kinetic energy spectra of double-shear-layer case at  $\tau = 50$ : comparison between the fourth-order SV algorithm, the fourth-order SV PPM algorithm, and the fifth-order SV algorithm with a fixed  $\Delta_f$  for the SV model. The first column presents the results using a  $64^3$  mesh with  $\Delta_f = \Delta x$ , while the second column uses a  $128^3$  mesh with  $\Delta_f = 2\Delta x$  and the third column uses a  $256^3$  mesh with  $\Delta_f = 4\Delta x$ . The first row presents the results in log-log form while the second row premultiplies the kinetic energy by the wavenumber,  $k$ , and presents the results in log-linear form to highlight the largest scales of the simulation. The dashed gray vertical line at  $k = 32$  in the plots of the first row displays the wavenumber at which the model is computed

But from the results presented in the second column of Fig. 5, it is seen that adding the SV model on top of the already existing numerical regularization does not significantly alter the results obtained using the stand-alone numerically regularized schemes presented in the last two rows of the first column of Fig. 5. To make sense of this, the form of the SV model must be considered. The model adds dissipation that is proportional in magnitude to the gradient squared. This is in contrast with methods that target only the highest frequency features in a simulation and are typically proportional to higher powers of the solution gradient. As a result, it is expected that the model dissipation affects more scales than just the smallest represented scales. The dissipation magnitude, however, is computed entirely using the smallest represented scales. When coupled with a small-scale-suppressing numerical regularization method, the SV model perceives almost no small scales

and therefore assumes almost no SGS kinetic energy. In essence, the SV model works entirely on the assumption that locally unresolved velocity gradients will exist in unresolved turbulent flows, which is not always the case when numerical regularization techniques are used in the simulation. From the LES point-of-view, the numerical regularization techniques used in this study increase the effective filter width of the complete LES system. To include the SV model in the system in a scheme-consistent manner, the model terms must be computed at the proper effective filter width.

As seen in column three of Fig. 5, when the SV model is computed at a coarser scale than the base mesh ( $\Delta_f > \Delta x$ ) as proposed in the present study, the results display less variation across all scales than when the coarsening is not utilized. This phenomenon occurs independent of the scheme tested, but is most pronounced in the numerically regularized cases. To compare the impact of all schemes, Fig. 6 compiles the results on one plot for each base mesh size. Figure 6 convincingly demonstrates scheme-independent simulations over coarse and medium turbulent scales using the SV model and numerical regularization. Engineering analysis often only considers larger-scale dynamics and it is encouraging that by increasing  $\Delta_f$ , these dynamics converge to the same result independent of the numerical regularization that is applied. Note that the result of the third column of Fig. 6 is not necessarily the most accurate for this case (e.g. a smooth flow). The most accurate solution is probably that using mesh  $256^3$  from the first row and column of Fig. 5. However, for flows with discontinuities, limiting or other stabilization must be added and the approach used for Fig. 6 becomes highly attractive.

## 5.2 Infinite-Reynolds-Number Taylor-Green Vortex

Results of the infinite-Reynolds-number Taylor-Green vortex case are presented in Fig. 7–9, with Fig. 7 demonstrating the kinetic energy spectrum fill-in over time and Fig. 8–9 showing the kinetic energy spectrum at  $\tau = 20$ .

As was mentioned in Section 4.4, the high-frequency information contained in the inviscid Taylor-Green vortex energy spectrum completely fills in by  $\tau \approx 10$  as shown in Fig. 7. After the high-frequency information is fully developed, the spectrum begins to decay away rather uniformly at the highest frequencies, while the lowest frequencies decay rather non-uniformly into the higher frequencies. The straight, temporally self-similar form of the energy spectrum is expected to continue at higher mesh resolutions and later simulation times due to the lack of physical dissipation.

Just as was seen in the previous test case, the results shown in column one of Fig. 8 lack large-scale grid-independence. The last two methods of numerical regularization seen in the first column are typical of implicit LES schemes used to simulate physically complex, high-Reynolds-number flows. In cases of extremely-high-Reynolds-number flows, where DNS results are impractical or impossible to obtain, difficulties arise when attempting to determine the quality of the implicit LES results. A reasonable expectation is for convergence in medium to large scale features as the grid is refined. This metric is used to judge the quality of the simulations in a meaningful way. As for the previous case, the fourth-order SV scheme shown in the first column of the first row exhibits less overall variation with decreasing  $\Delta x$ .

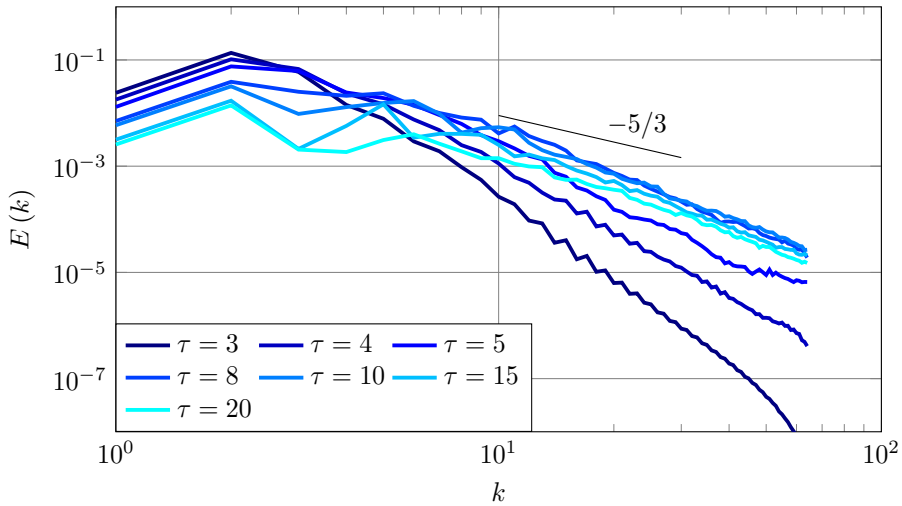


**Fig. 7** The inviscid Taylor-Green vortex energy spectrum time-evolution from the fourth-order centered scheme using the SV model and no numerical regularization with  $\Delta_f = \Delta x$  on a  $128^3$  mesh

In contrast with the temporally-evolving shear-layer, column two of Fig. 8 shows some improvement in large-scale consistency when the SV model is coupled with the numerical regularization techniques. While the fifth-order discretization shows the most improvement from adding the SV model, the fourth-order PPM scheme shows some improvement as well. As this is an inviscid, infinite-Reynolds-number case, it is expected that the numerical regularization will not eliminate all energy at the smallest representable scales. For example, if one considers a highly-compressible flow simulation which contains strong shocks, it will be noted that the smallest representable scales still contain significant energy, even with the use of numerical regularization. The SV model can still detect small-scale energy and use this to alter the large-scale information over time. As described in the temporally-evolving shear-layer case, it is expected that matching the LES filter width to the equivalent filter size of the numerical method would provide an even greater improvement in the results. These test cases are described next.

Column three of Fig. 8 shows the significant improvement provided by the coarsening method. For all three schemes tested, grid-independent LES solutions are obtained with all  $128^3$  results nearly identical to  $256^3$  results. The term “grid-independent solutions” is used here in the sense that the numerical errors have been isolated from the SV model effects. Clearly, the grid-independence being seen is due to an increase in grid resolution while introducing little or no new physics to the flow field. Another form of grid-independence would be to fix the filter width with respect to the discretization size and obtain converged solutions even as new physics at smaller scales are introduced to the simulation with an increasing mesh resolution. Ultimately, one expects convergence to DNS. Such a study evaluates both the model and its overall interaction with the CFD scheme. Similar to Chung

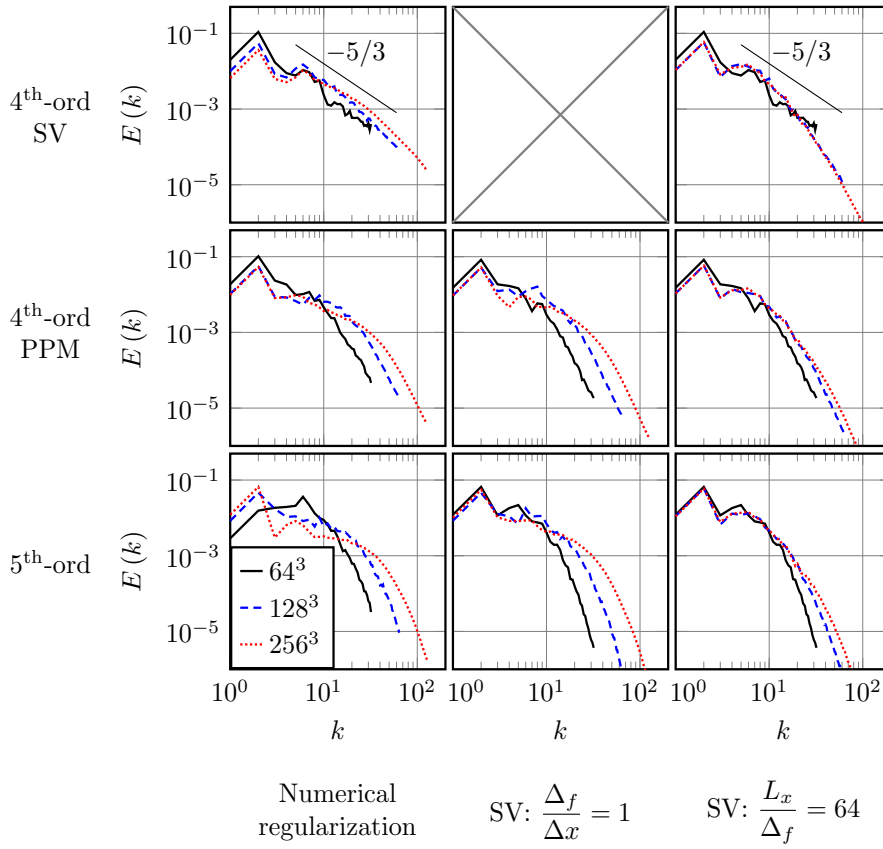


**Fig. 8** The inviscid Taylor-Green vortex kinetic energy spectrum at  $\tau = 20$ . The first column presents three methods of numerical regularization: the SV model (row 1), the PPM method (row 2), and biased interpolation (row 3). The second column adds the SV model to the PPM method (row 2), and the biased interpolation (row 3). The final column presents the same schemes except with a fixed  $\Delta_f$  equivalent to  $1/64^{\text{th}}$  the length of the domain

and Mattheou [30], the current study does not perform such a grid-independence test.

Figure 9 displays scheme-independent results as were seen in the previous test case. The near complete agreement between the large scales of Fig. 9 points to the success of the SV model in properly regularizing high-Reynolds-number turbulent flows and to independence from additional numerical regularization.

This particular case demonstrates that large-scale scheme-independence of high-Reynolds-number cases is achievable and that the effect of LES SGS models can be isolated without using an explicit-filtering approach. It is also possible that other structural LES SGS models could be used with the coarsening method presented here to obtain similar grid-independent results. With care, this method could be computationally less expensive than traditional explicit filtering methods

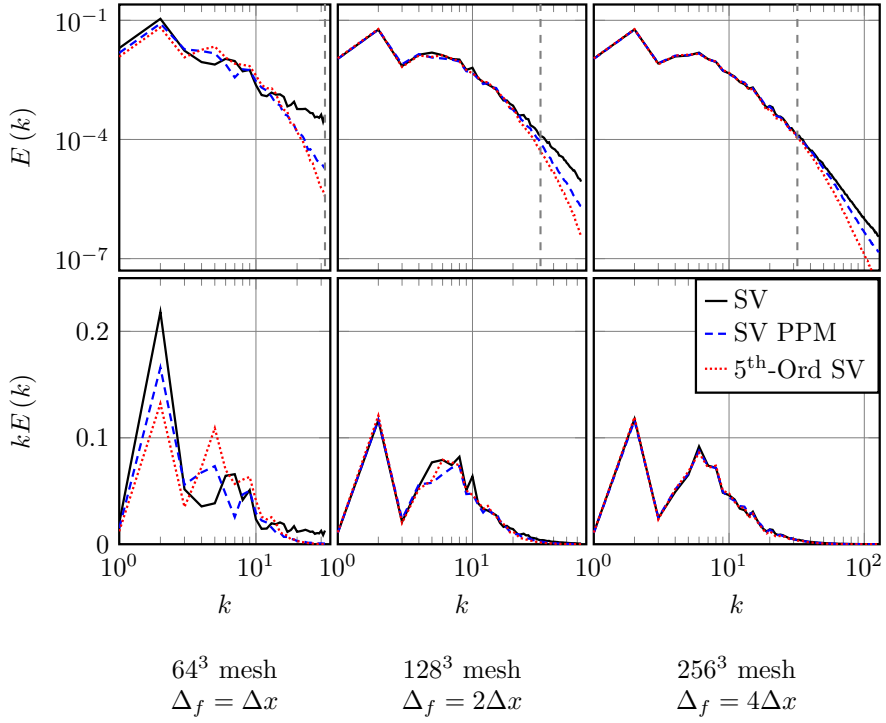


**Fig. 9** Inviscid Taylor-Green vortex kinetic energy spectrum at  $\tau = 20$ : comparison between the fourth-order SV algorithm, the fourth-order SV PPM algorithm, and the fifth-order SV algorithm with a fixed  $\Delta_f$  for the SV model. The first column presents the results using a  $64^3$  mesh with  $\Delta_f = \Delta x$ , while the second column uses a  $128^3$  mesh with  $\Delta_f = 2\Delta x$  and the third column uses a  $256^3$  mesh with  $\Delta_f = 4\Delta x$ . The first row presents the results in log-log form while the second row premultiplies the kinetic energy by the wavenumber,  $k$ , and presents the results in log-linear form to highlight the largest scales of the simulation. The dashed gray vertical line at  $k = 32$  in the plots of the first row displays the wavenumber at which the model is computed

used to evaluate LES SGS model performance. Instead of computing nonlinear model terms on the base mesh and then filtering the results, the model terms are naturally filtered when they are computed on the coarser mesh, leading to a reduction in the number of necessary computational evaluations. Utilized in the setting of a high-Reynolds-number turbulent flow, this method has the potential to provide an ideal test framework for the performance of various LES SGS models.

### 5.3 Decaying Homogeneous Turbulence

Results of the decaying, homogeneous turbulence case are presented in Fig. 10–11 which display the three-dimensional kinetic energy spectra at times corresponding

with the experimental measurement stations. Figure 10 presents the kinetic energy premultiplied by the wavenumber,  $k$ , in log-linear format so as to accentuate the larger scales of the simulation. Figure 11 compares the various schemes tested using a  $\Delta_f$  fixed at an equivalent resolution of  $64^3$ .

As stated in Section 1, the current study aims to obtain results showing scheme-independence and grid-independence (if possible) while using both the SV model and numerical regularization. Even for low-Reynolds-number turbulent flows it may be necessary to incorporate numerical regularization in cases where strong discontinuities exist and where the physics is particularly vigorous as in reacting turbulent flows. While the current test case is not reacting and does not require numerical regularization, future studies of low-Reynolds-number reacting flows will require regularization. As a result, this case continues the pattern of the previous test cases in scrutinizing the coupling of the SV model with various numerically regularized algorithms.

Similar to the previous two test cases, column one of Fig. 10 demonstrates that the fourth-order PPM method and the fifth-order interpolation display significant variation in the large scales with changing mesh resolution. Additionally, given the experimental data, it is apparent that numerical regularization techniques tested here remove spurious high-frequency solution content while simultaneously retaining too much well-resolved kinetic energy. The resultant kinetic energy overshoot does decrease with increasing mesh resolution as would be expected, but it does not decrease to the point of matching the experimental data. In contrast to this finding is the result obtained with the fourth-order SV scheme. This scheme shows much greater consistency among the scales as mesh resolution changes and is generally much closer to the experimental data than either of the numerically regularized schemes in column one. The comparisons in the first column demonstrate failings of ILES for this case versus a well-developed SGS model.

As was demonstrated in the first test case, it is seen from the results of the second column of Fig. 10 that the naive coupling of the SV model with the fourth-order PPM method or with the fifth-order interpolation makes little to no difference as compared with the regularized schemes without the SV model. It is interesting to note that this was the case with both low and medium-Reynolds-number tests, while the infinite-Reynolds-number case showed some improvement when the SV model with  $\Delta_f = \Delta x$  was added to the other two methods of numerical regularization.

When examining the cases utilizing the coarsened SV model as shown in the third column of Fig. 10, a substantial improvement over the second column of Fig. 10 is noted. In these figures, it must be noted that the simulations have the grid cutoff in the dissipative range of the turbulent kinetic energy spectra, while the SV model is computed at a length scale in the inertial range of the kinetic energy spectra. When  $\Delta_f = \Delta x$ , the SV model well handles a filter cutoff in the dissipative range. Having  $\Delta_f > \Delta x$ ,  $\Delta_f$  in the inertial range, and  $\Delta x$  in the dissipative range is a curiosity of this case. The result of the third column of Fig. 10 clearly shows that this is not a significant cause for concern in the decaying, homogeneous turbulence case. The implications and effects of this will be more exhaustively studied in future work. Nevertheless, grid convergence is more apparent in column 3 versus column 2 for the solutions with numerical regularization.

Similar to the first two test cases, Fig. 11 shows that the coarsening method nearly achieves scheme-independent solutions when the separation between the

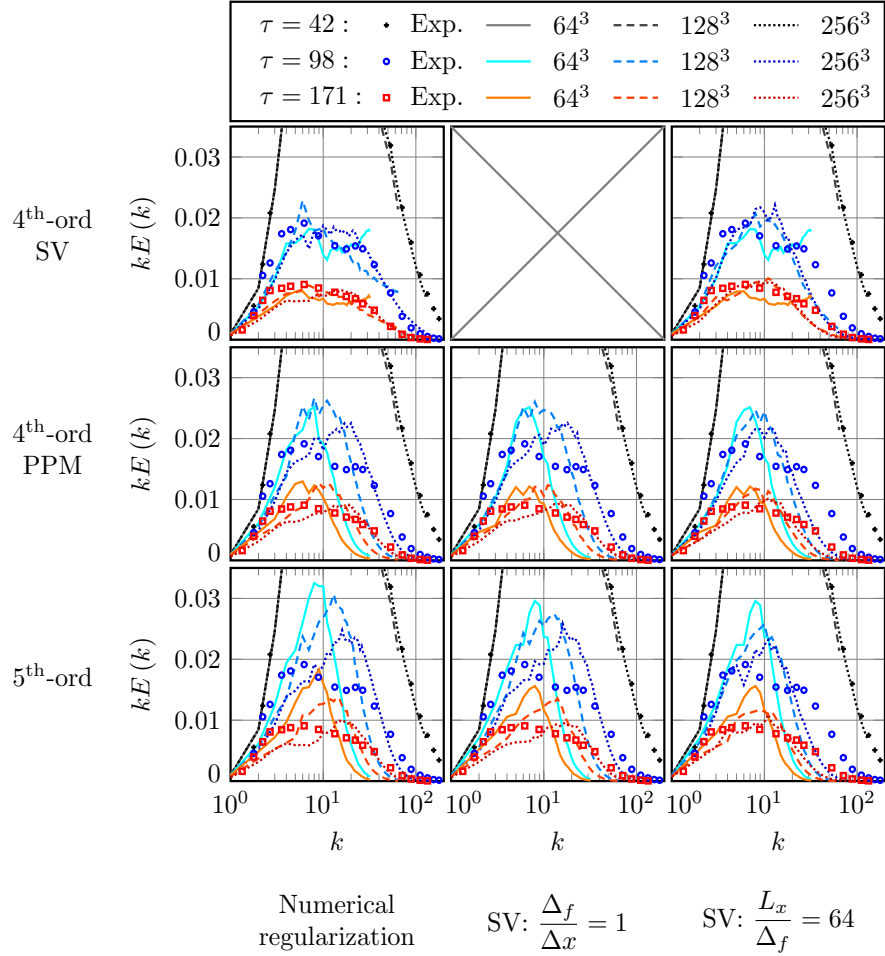


**Fig. 10** Kinetic energy spectrum for decaying homogeneous turbulence. The first column presents three methods of numerical regularization: the SV model (row 1), the PPM method (row 2), and biased interpolation (row 3). The second column adds the SV model to the PPM method (row 2), and the biased interpolation (row 3). The final column presents the same schemes as the second column except with a fixed  $\Delta_f$  equivalent to  $1/64^{\text{th}}$  the streamwise length of the domain. The initial conditions for  $\tau = 42$  are all identical to one another and are cropped to emphasize differences in the other time scales

numerical regularization and the SV model is sufficient to allow the SV model to operate appropriately. The results do show some small differences between the schemes even when  $\Delta_f = 4\Delta x$ . Even for relatively low-Reynolds-number decaying turbulence cases such as this, the coarsened SV model provides an improvement over the numerically regularized algorithms, used both with and without the SV model. Again, note that the bare SV model (row 1, column 1 of Fig. 10) best fits

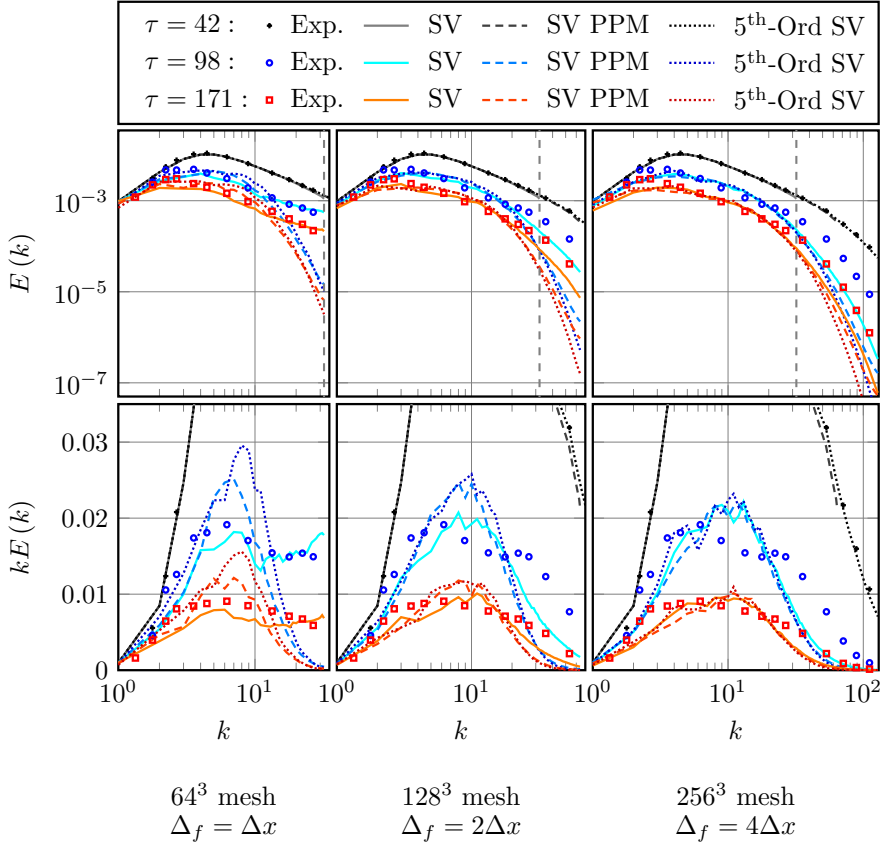


**Fig. 11** Kinetic energy spectrum for decaying homogeneous turbulence: comparison between the fourth-order SV algorithm, the fourth-order SV PPM algorithm, and the fifth-order SV algorithm with a fixed  $\Delta_f$  for the SV model. The first column presents the results using a  $64^3$  mesh with  $\Delta_f = \Delta x$ , while the second column uses a  $128^3$  mesh with  $\Delta_f = 2\Delta x$  and the third column uses a  $256^3$  mesh with  $\Delta_f = 4\Delta x$ . The first row presents the results in log-log form while the second row premultiplies the kinetic energy by the wavenumber,  $k$ , and presents the results in log-linear form to highlight the largest scales of the simulation. The dashed gray vertical line at  $k = 32$  in the plots of the first row displays the wavenumber at which the model is computed

the data. But if additional numerical regularization is necessary, there is strong evidence of scheme convergence and moderate evidence of grid convergence when the SV model is applied at coarser scales. The coarsening method proposed in the current study shows that even though the SV model was designed for high-Reynolds-number flows, it has the capability of working in rather low-Reynolds-number flows if properly coupled with the existing algorithmic components.

## 6 Conclusions

In the current study, it is shown that the new methodology of computing the SV model at a coarser scale than the base mesh achieves scheme-independence even when various numerical regularization techniques are included in the LES system. Additionally, grid-independence of the large scales (in the sense of isolating numerical error from model effects) is achieved for high-Reynolds-number flows. Furthermore, this methodology introduces a new avenue for discerning the impact of the SGS model and the numerical regularization on the solution. This new avenue may be more robust and reliable than using explicit filtering.

Within the present study, the interaction of the various algorithmic components was seen to heavily influence the final simulation outcome. When the methods of numerical regularization used in the present study are incorporated into simulations, they suppress the highest-frequency information and prevent the SV model from detecting sufficient SGS kinetic energy. However, when the SV model is evaluated at a coarser resolution than the base mesh, it is more isolated from the numerical regularization and can add the proper dissipation to all scales of the system.

The temporally-evolving shear-layer was seen to achieve scheme-independence for all scales when  $\Delta_f = 4\Delta x$ . It was also noted that the large-scale structures of the overall flow field remained the same as the  $\Delta_f/\Delta x$  ratio was increased.

In addition to the previously mentioned grid-independence, the infinite-Reynolds-number Taylor-Green vortex case showed some improvement of the solution when the SV model using  $\Delta_f = \Delta x$  was coupled with the fourth-order PPM method and the fifth-order interpolation scheme. This was the only case that showed this improvement before implementing the coarsening method described in this study. Given that the SV model was developed for high-Reynolds-number flows, it was not surprising that this test case showed the best results.

While the decaying homogeneous turbulence case did not perform as well as the first two test cases, it demonstrated significant improvement using the new methodology. The case nearly reached scheme-independence across all scales.

This methodology reduces the computational expense associated with computing the SGS model as it requires approximately  $3(\Delta_f/\Delta x)^3$  fewer evaluations of the actual SV model kinetic energy estimate. In the case of  $\Delta_f = 4\Delta x$ , this corresponds to two orders of magnitude fewer computational evaluations of the SGS kinetic energy estimate. The necessary averaging and interpolation operators add relatively little overhead as they are already an essential part of the functionality in the AMR framework used in the current study. However, this should not be construed as a reason to set  $\Delta_f > \Delta x$ . Rather, consider using  $\Delta_f > \Delta x$  only if additional numerical regularization is to be combined with the SV model.

The findings presented in the current study pave the way for appropriately incorporating the SV model into future studies of highly compressible, reacting, turbulent flows that contain strong discontinuities. Such studies have the potential to extend the new coarsening method to SV wall-models and provide a more consistent coupling between wall-models and freestream LES SGS models.

**Acknowledgements** The authors would like to acknowledge insightful discussions with Dr. Phillip Colella that contributed towards the methodologies proposed in this paper.

## Conflict of interest

The authors declare that they have no conflict of interest.

## Publication History

This paper was originally published online on 25 August 2020 by Springer Nature for the journal Flow, Turbulence and Combustion at <https://doi.org/10.1007/s10494-020-00206-1>. The final publication is available at link.springer.com.

## References

1. Pope, S.B.: Ten questions concerning the large-eddy simulation of turbulent flows. *New Journal of Physics* **6**, 1–24 (2004). DOI 10.1088/1367-2630/6/1/035
2. Sagaut, P.: Large Eddy Simulation for Incompressible Flows: An Introduction, 3rd edn. Springer-Verlag (1998)
3. Grinstein, F.F., Margolin, L.G., Rider, W.J.: Implicit Large Eddy Simulation: Computing Turbulent Fluid Dynamics, 1st edn. Cambridge University Press (2007)
4. Karaca, M., Lardjane, N., Fedioun, I.: Implicit Large Eddy Simulation of high-speed non-reacting and reacting air/H<sub>2</sub> jets with a 5th order WENO scheme. *Comput. Fluids* **62**, 25–44 (2012)
5. Fernandez, P., Nguyen, N.C., Peraire, J.: The hybridized discontinuous Galerkin method for implicit Large-Eddy Simulation of transitional turbulent flows. *J. Comput. Phys.* **336**, 308–329 (2017)
6. Moura, R.C., Mengaldo, G., Peiro, J., Sherwin, S.J.: On the eddy-resolving capability of high-order discontinuous Galerkin approaches to implicit LES/under-resolved DNS of Euler turbulence. *J. Comput. Phys.* **330**, 615–623 (2017)
7. Carton de Wiart, C., Hillewaert, K., Bricteux, L., Winckelmans, G.: Implicit LES of free and wall-bounded turbulent flows based on the discontinuous Galerkin/symmetric interior penalty method. *Int. J. Numer. Method. Fluids* **78**, 335–354 (2015)
8. Misra, A., Pullin, D.I.: A vortex-based subgrid stress model for large-eddy simulation. *Phys. Fluids* **9**(8), 2443–2454 (1997)
9. Gao, W., Zhang, W., Cheng, W., Samtaney, R.: Wall-modeled large-eddy simulation of turbulent flow past airfoils. *J. Fluid Mech.* **873**, 174–210 (2019)
10. Lundgren, T.S.: Strained spiral vortex model for turbulent fine structure. *Phys. Fluids* **25**(12), 2193–2203 (1982)
11. Chung, D., Pullin, D.I.: Direct numerical simulation and large-eddy simulation of stationary buoyancy-driven turbulence. *J. Fluid Mech.* **643**, 279–308 (2010)
12. Mattner, T.W.: A refined stretched-vortex model for large-eddy simulation of turbulent mixing layers. Tech. rep., 17th Australasian Fluid Mechanics Conference (2010)
13. Mattner, T.W.: Large-eddy simulations of turbulent mixing layers using the stretched vortex model. *J. Fluid Mech.* **671**, 507–534 (2011)
14. Walters, S., Guzik, S., Gao, X.: Evaluation of the stretched-vortex subgrid-scale model for large-eddy simulation with a fourth-order finite volume algorithm. In: 2019 AIAA SciTech Forum, AIAA 2019-1886. <https://doi.org/10.2514/6.2019-1886>
15. Voelkl, T., Pullin, D.I., Chan, D.C.: A physical-space version of the stretched-vortex subgrid-stress model for large-eddy simulation. *Phys. Fluids* **12**(7), 1810–1825 (2000)
16. Chung, D., Pullin, D.I.: Large-eddy simulation and wall modelling of turbulent channel flow. *J. Fluid Mech.* **631**, 281–309 (2009)
17. Shetty, D.A., Frankel, S.H.: Assessment of stretched vortex subgrid-scale models for LES of incompressible inhomogeneous turbulent flows. *Int. J. Numer. Meth. Fluids* **73**, 152–171 (2013)
18. Kosovic, B., Pullin, D.I., Samtaney, R.: Subgrid-scale modeling for large-eddy simulations of compressible turbulence. *Phys. Fluids* **14**(4), 1511–1522 (2002)
19. Hill, D.J., Pantano, C., Pullin, D.I.: Large-eddy simulation and multi-scale modelling of a Richtmyer-Meshkov instability with reshock. *J. Fluid Mech.* **557**, 29–61 (2006)

20. Gao, X., Guzik, S.M.J., Colella, P.: Fourth order boundary treatment for viscous fluxes on Cartesian grid finite-volume methods. AIAA 2014-1277, 52nd AIAA Aerospace Sciences Meeting (2014)
21. Guzik, S.M., Gao, X., Owen, L.D., McCorquodale, P., Colella, P.: A freestream-preserving fourth-order finite-volume method in mapped coordinates with adaptive-mesh refinement. *Comput. Fluids* **123**, 202–217 (2015)
22. Guzik, S.M., Gao, X., Olschanowsky, C.: A high-performance finite-volume algorithm for solving partial differential equations governing compressible viscous flows on structured grids. *Comput. Math Appl.* **72**, 2098–2118 (2016)
23. Gao, X., Owen, L.D., Guzik, S.M.J.: A parallel adaptive numerical method with generalized curvilinear coordinate transformation for compressible Navier-Stokes equations. *Int. J. Numer. Meth. Fluids* **82**, 664–688 (2016)
24. Owen, L.D., Guzik, S.M., Gao, X.: A high-order adaptive algorithm for multispecies gaseous flows on mapped domains. *Comput. Fluids* **170**, 249 – 260 (2018)
25. Colella, P., Graves, D.T., Keen, N., Ligocki, T.J., Martin, D.F., McCorquodale, P., Modiano, D., Schwartz, P., Sternberg, T., Straalen, B.V.: Chombo Software Package for AMR Applications - Design Document. Lawrence Berkeley National Laboratory (2009). <https://seesar.lbl.gov/anag/chombo/ChomboDesign-3.0.pdf>
26. Colella, P., Sekora, M.: A limiter for PPM that preserves accuracy at smooth extrema. *J. Comput. Phys.* **227**(15), 7069–7076 (2008)
27. McCorquodale, P., Colella, P.: A high-order finite-volume method for conservation laws on locally refined grids. *Comm. App. Math. Comput. Sci.* **6**(1), 1–25 (2011)
28. Chaplin, C., Colella, P.: A single-stage flux-corrected transport algorithm for high-order finite-volume methods. *Communications in Applied Mathematics and Computational Science* **12**(1), 1–24 (2017). DOI <https://doi.org/10.2140/camcos.2017.12.1>
29. Colella, P., Woodward, P.R.: The piecewise parabolic method PPM for gas-dynamical simulations. *J. Comput. Phys.* **54**, 174–201 (1984)
30. Chung, D., Matheou, G.: Large-eddy simulation of stratified turbulence. part i: A vortex-based subgrid-scale model. *Journal of the Atmospheric Sciences* **71**, 1863–1879 (2014)
31. Pantano, C., Sarkar, S.: A study of compressibility effect in the high-speed turbulent shear layer using direct simulation. *J. Fluid Mech.* **451**, 329–371 (2002)
32. Jackson, T.L., Grosch, C.E.: Absolute/convective instabilities and the convective mach number in a compressible mixing layer. Tech. rep., NASA (1989)
33. Bull, J.R., Jameson, A.: Simulation of the compressible taylor green vortex using high-order flux reconstruction schemes. In: 7th AIAA Theoretical Fluid Mechanics Conference, AIAA 2014-3210. AIAA Aviation Forum (2014)
34. Comte-Bellot, G., Corrsin, S.: Simple Eulerian time correlation of full and narrow-band velocity signals in grid-generated, 'isotropic' turbulence. *J. Fluid Mech.* **48**, 273–337 (1971)
35. Skeledzic, T., Krauss, J., Lienhart, H., Ertunc, Ö., Jovanovic, J.: Characterization of turbulence generated by an active grid with individually controllable paddles. In: New Results in Numerical and Experimental Fluid Mechanics XI, pp. 105–114. Springer International Publishing, Cham (2018)
36. Hearst, R.J., Lavoie, P.: The effect of active grid initial conditions on high reynolds number turbulence. *Experiments in Fluids* **56**(10), 185 (2015)
37. Rozema, W., Bae, H.J., Moin, P., Verstappen, R.: Minimum-dissipation models for large-eddy simulation. *Phys. Fluids* **27**, 085107 (2015)
38. Kang, H.S., Chester, S., Meneveau, C.: Decaying turbulence in an active-grid-generated flow and comparisons with large-eddy simulation. *J. Fluid Mech.* **480**, 129–160 (2003)